

SiQDs-mediated highly efficient hole transfer for photocatalytic overall water splitting over Cu-doped ZnIn₂S₄

Wenwen Shi ^a, Baoxin Ge ^a, Pengyang Jiang ^a, Qiaoyun Wang ^a, Lifeng He ^b, Caijin Huang ^{a,b,*}

^a State Key Laboratory of Photocatalysis on Energy and Environment, College of Chemistry, Fuzhou University, Fuzhou 350108, PR China

^b College of Maynooth International Engineering, Fuzhou University, Fuzhou 350116, PR China



ARTICLE INFO

Keywords:

Photocatalytic overall water splitting
SiQDs
Hole transfer
ZnIn₂S₄

ABSTRACT

Sluggish hole transfer and the resulting pronounced charge recombination hinder the efficiency of photocatalytic overall water splitting. Herein, we present Si quantum dots (SiQDs) as hole transporter to construct SiQDs/Cu-doped ZnIn₂S₄ heterojunction photocatalysts (Cu_{0.48}SZ) for overall water splitting. Under visible light illumination, Cu_{0.48}SZ exhibits highly stable overall water-splitting activity of 210 $\mu\text{mol g}^{-1} \text{h}^{-1}$ H₂ and 97 $\mu\text{mol g}^{-1} \text{h}^{-1}$ O₂ with an apparent quantum yield (AQY) of 2.57 % at 420 nm. Results demonstrate that the synergy of SiQDs and Cu doping enhances carrier-separation efficiency and reduce surface kinetic barriers, leading to high photocatalytic performance. The presence of SiQDs effectively accelerates the transfer of photoexcited holes and avoids the self-oxidation of ZnIn₂S₄, favoring water oxidation. The Cu doping increases the electron density around the S atoms of ZnIn₂S₄ and thus promotes water reduction. This work extends the application of SiQDs as efficient hole transporter for photocatalytic overall water splitting.

1. Introduction

Photocatalytic hydrogen production from water has been considered as a low-cost and sustainable way to convert solar energy to clean hydrogen energy [1,2]. In the past decades, the vast majority of research on photocatalytic water splitting has focused on the more facile half-reaction of hydrogen evolution reaction (HER) using sacrificial agents to scavenge photogenerated holes, which greatly reduces its potential for industrial applications [3–5]. In fact, photocatalytic overall water splitting is limited by the thermodynamic contradiction between redox potentials and the more difficult half-reaction of oxygen evolution reaction (OER) [6–8]. The main challenges in boosting OER include the four-electron pathway of water splitting to oxygen, accumulation of photogenerated holes and slow surface redox kinetics [9,10]. For most semiconductors, since electrons have much smaller effective mass than holes, the migration rate of holes is relatively slow, resulting in the accumulation of photoinduced holes. This slows the OER process and then the entire water-decomposition process. Therefore, how to prompt the hole-transfer process and optimize hole utilization is the key to achieve highly efficient photocatalytic overall water splitting [11–13].

In recent years, many semiconductor photocatalysts, such as TiO₂, g-

C₃N₄, ZnIn₂S₄ (ZIS), have been extensively used for photocatalytic overall water splitting [14–16]. Among them, ZIS possesses strong visible-light response ability and appropriate band structure for driving both water oxidation and reduction reactions, and has gained significant attention [17]. However, single-phased ZIS photocatalysts also suffer from difficulties in overall water-splitting performance due to the low electron–hole separation efficiency and self-oxidation caused by hole accumulation [18]. To address this issue, some strategies including morphology regulation, cation exchange, elemental doping, defect engineering, co-catalyst loading, and heterojunction construction have been developed to improve the overall water splitting performance of ZIS-based photocatalysts [19–23]. Boosting photoexcited hole transfer is one of the most important means to increase the OER activity of ZIS, which can be realized by quickly transferring the holes to the appropriate reaction sites via cocatalysts for water oxidation and further avoiding severe self-photocorrosion [24]. Recently, carbon dots (CDs) have been proved to be good hole transporters for prompting the photocatalytic activity [25]. For example, Wu et al. used CDs to capture and transfer photogenerated holes to promote the BA-oxidation-coupled hydrogen evolution activity [26]. Similar to CDs, silicon quantum dots (SiQDs) exhibit optical/electronic properties and light stability that are

* Corresponding author at: State Key Laboratory of Photocatalysis on Energy and Environment, College of Chemistry, Fuzhou University, Fuzhou 350108, PR China.

E-mail address: cjhuang@fzu.edu.cn (C. Huang).

more unique than their bulk phase and have great potential in the field of optoelectronic devices and catalysts [27–29]. So far, there have been few applications of SiQDs as a metal-free photo-cocatalyst, which inspires us to design a hybrid SiQDs/ZIS photocatalyst to obtain high OER activity.

HER activity can be effectively enhanced by elemental doping through cation exchange, which can facilitate charge transport and construct rich active sites for water reduction. Cation exchange reaction presents a process of replacing host cations by foreign mobile cations, rendering the almost unchanged anion framework. Besides, the change of electronic structure by the guest atoms themselves greatly promotes the charge separation and transfer by tuning the electronic properties of the neighboring atoms, which is also beneficial for HER [30–32]. Among various cation exchange, Cu-doped photocatalyst (e.g., ZnS/CuS, Cu-In-Zn-S) has been attractive for solar-to-hydrogen conversion owing to their tunable band structures and environmental benignity [33,34]. Wang et al. constructed ZnIn₂S₄@CdIn₂S₄ heterojunction with high photocatalytic efficiency through a spatially selective cation exchange synthesis approach [35].

In this work, we construct SiQDs/Cu-doped ZnIn₂S₄ (Cu_xSZ) composite photocatalysts by hydrothermal method and cation exchange. The presence of SiQDs facilitates the efficient transfer of photogenerated holes for water oxidization and improves the stability of ZIS. The Cu²⁺ doping enhances the ability of visible light harvesting and H⁺ adsorption for water reduction. Benefiting from the synergistic effects of SiQDs and Cu doping, the sample Cu_{0.48}SZ achieved stable and stoichiometric H₂- and O₂- evolution rates under visible-light irradiation and a high apparent quantum yield (AQY). Finally, through experimental and theoretical investigations, we demonstrate the crucial role of SiQDs and Cu doping in the photocatalytic process and the reaction mechanism.

2. Experimental section

2.1. Chemicals

Anhydrous zinc chloride (ZnCl₂) was obtained from Macklin. Indium nitrate hydrate (InCl₃•4 H₂O), thioacetamide (C₂H₅SN, TAA), cupric nitrate trihydrate (Cu(NO₃)₂•3 H₂O), Tri-sodium citrate (C₆H₇Na₃O₈) and anhydrous ethanol (C₂H₆O) were supplied by Sinopharm Chemical Reagent Co. Ltd. Triethoxysilane (C₉H₂₃O₃NSi, APTES), 5,5-dimethyl-1-pyrroline N-oxide (DMPO) and N, Ndimethylformamide (C₃H₇NO, DMF) were purchased from Aladdin Biological Technology Co. Ltd. Xinhang Gas Co. Ltd. provided argon gas (Ar) with 99.9 % purity.

2.2. Synthesis

2.2.1. Synthesis of SiQDs

SiQDs colloid was synthesized according to the previous report with some modifications [36]. Tri-sodium citrate (0.9 g) was dissolved in 20 mL deionized water and run through nitrogen gas for 15 min. 5 mL APTES was added into the solution under stirring. The mixture was sealed in a 50 mL Teflon-lined and heated at 200 °C for 5 h. The SiQDs product was filtered through a 0.22-micron membrane and stored at 4 °C. The as-obtained SiQDs emit intense blue fluorescence under 365 nm UV light and show typical excitation-wavelength-dependent fluorescence behavior (Fig. S6), which is a feature of QDs [37].

2.2.2. Synthesis of SiQDs/ZIS

Typically, ZnCl₂ (0.1363 g) and InCl₃•4 H₂O (0.5864 g) were added into 20 mL of ethanol. The as-obtained SiQDs solution (1 mL) and thioacetamide (0.3 g) was added into the above mixture in turn, where thioacetamide serves as sulfur source. The mixture was sealed in a 50 mL Teflon-lined stainless-steel autoclave and heated at 120 °C for 2 h. The product was centrifugally washed with deionized water and ethanol and dried at 60 °C in a vacuum oven. The SiQDs/ZnIn₂S₄ product was labelled as SiQDs/ZIS. ZnIn₂S₄ (ZIS) sample was prepared as the above

procedures without SiQDs. The photographs of ZIS and SiQDs/ZIS are given in Fig. S1.

2.2.3. Synthesis of Cu_xSZ

SiQDs/Cu-doped ZIS composites were obtained by cation exchange method. First, 50 mg SiQDs/ZIS and 0.01 M Cu (NO₃)₂•3 H₂O solution were dispersed in 25 mL of deionized water under stirring. The mass ratio of Cu to SiQDs/ZIS ranges from 0.27 to 0.69 wt% (0.27, 0.38, 0.48, 0.58, 0.69 wt%) by adding different volumes of 0.01 M Cu (NO₃)₂ solution. The product was collected by vacuum filtration, washed with deionized water, and dried in a vacuum oven at room temperature. The product was labeled as Cu_xSZ where x represents the mass ratio of Cu to SiQDs/ZIS. The photograph of Cu_{0.48}SZ was shown in Fig. S1c.

2.3. Characterizations

X-ray diffraction (XRD) patterns were obtained using X-ray diffractometer (Bruker, D8 Advance, Cu K α irradiation). Morphology analyses were performed by scanning electron microscopy (SEM, Hitachi SU-8010). Transmission electron microscopy (TEM) results were taken through FEI electron microscope (Talos F200X). X-ray photoelectron spectroscopy (XPS) measurements were conducted on an X-ray photoelectron spectrometer (Thermo Scientific) using monochromatic Al K α as the X-ray source. Raman spectra were measured using a Renishaw inVia Raman microscope. BET surface areas were calculated by the Brunauer–Emmett–Teller (BET) method. Pore-size distributions were analyzed by the BJH method. UV-vis diffuse reflectance spectra (DRS) were performed on a Cary5000 Scan UV-vis-NIR spectrometer (Agilent) with BaSO₄ as the reference. Photoluminescence (PL) spectra were recorded on a HORIBA Fluorolog-3-TCSPC spectrophotometer under 280 nm excitation. Time-resolved PL (TRPL) spectra were acquired on a HORIBA DeltaPro. Surface photovoltage (SPV) spectra were performed on a device including a 500 W Xe lamp equipped with a monochromator, a photovoltaic cell, a signal processor and a light-chopper-assisted lock-in amplifier. Electron paramagnetic resonance (EPR) data were collected using a Bruker A300 spectrometer at room temperature. Contact angle measurements were conducted on a Contact Angle Meter OCA50.

2.4. Photo-electrochemical measurements

All photo-electrochemical properties were measured on an electrochemical workstation (SAS SP-300, Bio-Logic) using a standard three-electrode system. In the typical three-electrode system, Pt and Ag/AgCl (saturated KCl) act as the counter electrode and reference electrode, respectively. The typical working electrode was prepared as follows: 10 mg catalyst was dispersed into 0.5 mL of DMF solution and 20 μ L of Nafion. Then, the catalyst dispersion (20 μ L) was deposited on the conductive area of the FTO glass (active area: 0.28 cm²) and dried in air at room temperature. The electrolyte was 0.2 M Na₂SO₄ aqueous solution. The Mott–Schottky plots were obtained using a bias potential ranging from 0 to 1 V under different frequencies of 0.5, 1, and 1.5 kHz, respectively. Electrochemical impedance spectroscopy (EIS) was tested at open-circuit potential with a frequency range of 10⁻² to 10⁵ Hz and 10 mV AC amplitude. The photocurrent-time (i-t) curves were conducted under 300 W Xe lamp irradiation at 0.2 V bias voltage.

The potentials measured by Ag/AgCl (sat. KCl) can be converted to the reversible hydrogen electrode (RHE) according to the Nernst Equation:

$$E_{\text{RHE}} = E_{\text{Ag/AgCl}} + 0.197 \text{ V} + 0.0591 \times \text{pH}$$

2.5. Photocatalytic measurements

Photocatalytic tests were performed in a 500 mL quartz photoreactor

with an online photocatalytic analysis system (Labsolar-IIAG, Beijing Perfectlight). Typically, the as-prepared photocatalyst (10 mg) was dispersed into pure water (50 mL), and then transferred to the reactor. The reaction system was exhausted to remove air. A 300 W Xenon lamp (CELHXF300, CEAULIGHT, China) with a 420 nm long-pass cutoff filter was used as light source. The reaction temperature was maintained at 25 °C by circulating cooling water. Finally, the amount of evolved gas was analyzed by gas chromatograph (FULI 9750, TCD detector, argon carrier gas). The apparent quantum yield (AQY) was evaluated using four LED lamps (365, 420, 460, and 520 nm) as light sources. The irradiation area is about 3.14 cm². The AQY was calculated according to the following equation:

$$\text{AQY}(\%) = \frac{2 \times \text{number of evolved H}_2 \text{ molecules}}{\text{number of incident photons}} \times 100$$

$$= \frac{2 \times n_{H_2} \times N_A \times h \times c}{S \times P \times t \times \lambda} \times 100\%$$

Where n_{H_2} represent the moles of H₂; N_A is Avogadro constant; h is Planck constant; c is lightspeed; S represents the irradiation area; P represents the average incident light intensity; t is the reaction time; λ is irradiation wavelength.

2.6. Computational details

The density functional theory (DFT) calculations were executed on Vienna ab initio simulation package (VASP) [38]. The projected augmented wave (PAW) method was employed to characterize the interaction between ions and electrons [39]. The exchange-correlation

functional was described using the Perdew–Burke–Ernzerh (PBE) form of the generalized gradient approximation (GGA). The geometry relaxation continued until all atoms experienced a residual force below 0.01 eV/Å. The PAW potentials employed the frozen core orbital approximation. For all calculations, a 4 × 4 × 1 supercell with a gamma-centered k-grid of 3 × 3 × 1 was employed, unless stated otherwise. Charge transfer between adatoms and ZnIn₂S₄ monolayer was analyzed using Bader charge approach [40].

Zero-point energy (ZPE) and entropy (S) adjustments correct the free energy of adsorption:

$$G = E + ZPE - TS$$

where the ZPE and S can be derived from the vibrational frequency calculations of the adsorbed species with temperature (T) set at 298.15 K.

The OER overpotential (η_{OER}) was obtained using [41]:

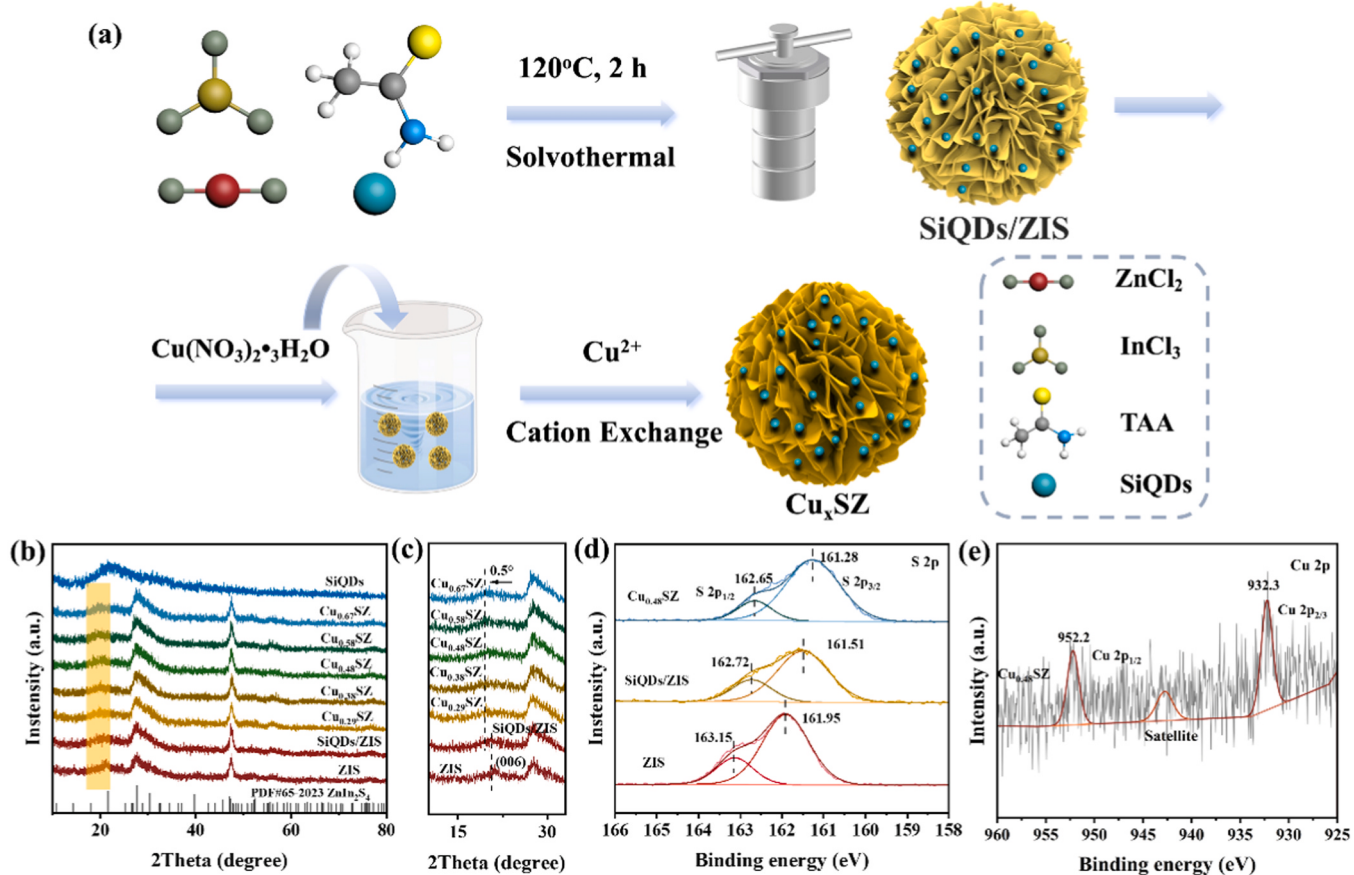
$$\eta_{OER} = \max(\Delta G_1, \Delta G_2, \Delta G_3, \Delta G_4)/e - 1.23$$

where $\max(\Delta G_1, \Delta G_2, \Delta G_3, \Delta G_4)$ means the step with the greatest energy output from the four, identified as the potential-determining step (PDS).

3. Results and discussion

3.1. Catalyst synthesis and characterization

Fig. 1a depicts the synthetic process of SiQDs/Cu-ZIS (Cu_xSZ) via a facile one-pot solvothermal method and cation exchange. The XRD patterns of SiQDs/ZIS and Cu_xSZ still exhibit the characteristic peaks of



hexagonal $ZnIn_2S_4$ (Fig. 1b). Due to the presence of the peak around 21.6° for SiQDs, the (006) plane of ZIS located at 21.2° becomes widening and shifts towards a lower angle in SiQDs/ZIS, implying the strong interaction between ZIS and SiQDs [42]. For the Cu_xSZ samples, the diffraction peak at 20.4° corresponding to the (006) plane of ZIS shifts toward a lower angle (Fig. 1c), indicating that the copper element was successfully incorporated and this process does not introduce a comparative amount of impurities [32].

Fig. S3a shows the survey XPS spectra of the samples. In Figs. S3b, c and Fig. 1d, the binding energies of Zn 2p (1022.25 and 1045.35 eV), In 3d (445.10 and 452.60 eV), and S 2p (161.95 and 163.15 eV) of pure ZIS are attributed to Zn^{2+} , In^{3+} , and S^{2-} ions, respectively [43]. The introduction of SiQDs onto ZIS makes Zn 2p, In 3d and S 2p a negative shift (Fig. S3d), manifesting interfacial electron transfer from SiQDs to ZIS and the subsequent formation of a built-in electric field at the interface of SiQDs/ZIS [44]. The heterojunction between ZIS and SiQDs is favorable for the separation/migration of photoinduced charges and spatially separated redox reactions during photocatalysis. As a result, the positive charges tend to accumulate on SiQDs, which is helpful to the absorption of H_2O molecules and thus boosts the OER process [24]. In addition, a satellite peak appears within the two peaks at 932.30 (Cu 2p_{3/2}) and 952.20 eV (Cu 2p_{1/2}), demonstrating the existence of Cu^{2+} in $Cu_{0.48}SZ$ (Fig. 1e) [45]. The peaks of S 2p have an obvious positive shift after Cu^{2+} doping in SiQDs/ZIS, meaning that more electrons gathered around S atoms after partial substitution of Zn by Cu, which is more favorable for H^+ adsorption in the HER process.

All ZIS-containing samples have uniform morphologies of nanosheet-assembled flower-like microspheres, but SiQDs/ZIS and $Cu_{0.48}SZ$ present looser structure than ZIS (Fig. 2a, b and Fig. S4). The looser structure is advantageous in exposing more active surface, which is also confirmed by the specific surface areas through N_2 gas adsorption/

desorption analysis (Fig. 2c). Besides, the N_2 adsorption–desorption isotherms of ZIS, SiQDs/ZIS and $Cu_{0.48}SZ$ give a main pore diameter of about 4.4 nm (Fig. S5), which ensures migration of H_2O molecules. From TEM images (Fig. 2d and Fig. S6), pure SiQDs exhibit an average diameter of 5.0 ± 0.5 nm and a clear lattice spacing of 0.30 nm corresponding to the (111) plane of Si crystals [46]. Fig. 2e, f shows the sheet-assembled structure of highly dispersed $Cu_{0.48}SZ$. The HRTEM images of $Cu_{0.48}SZ$ display the (102) plane of ZIS and the Si (111) plane of SiQDs [47]. The elemental mapping images demonstrate the homogeneous dispersion of Si and Cu elements in $Cu_{0.48}SZ$ (Fig. 2h-m and Fig. S7). The Si mass fraction in $Cu_{0.48}SZ$ was calculated to be 2.37 % from the EDS spectrum (Fig. S8 and Table S1). The real Cu mass fraction in $Cu_{0.48}SZ$ detected by ICP was 0.25 wt% (Table S2). Moreover, the results given in Table S3 reveal that the weight percent of Zn decreases rapidly with increasing Cu dopant concentration, while the weight percent of In remains almost unchanged, implying that Cu atoms selectively replace Zn atoms.

3.2. Photocatalytic performance for water splitting

Photocatalytic overall water splitting experiments were performed in pure water under visible light irradiation ($\lambda \geq 420$ nm) without any sacrificial agent (Fig. S9). Pure ZIS shows a low and unstable H_2 -evolution activity ($8 \mu\text{mol g}^{-1} \text{h}^{-1}$) without any O_2 evolution (Fig. S10a). The Cu doping obviously increases the HER activity of ZIS, but still does not improve the stability and OER activity (Fig. S10b). The unstable HER activity of ZIS and $Cu_{0.48}$ -ZIS is possibly due to the self-oxidation of ZIS caused by the accumulation of photoexcited holes [48]. However, by loading SiQDs onto ZIS, the composites exhibit enhanced, stable and stoichiometric HER and OER activity (Fig. S11). For comparison, no any HER/OER activity was found for pure SiQDs (Fig. 4a). These results

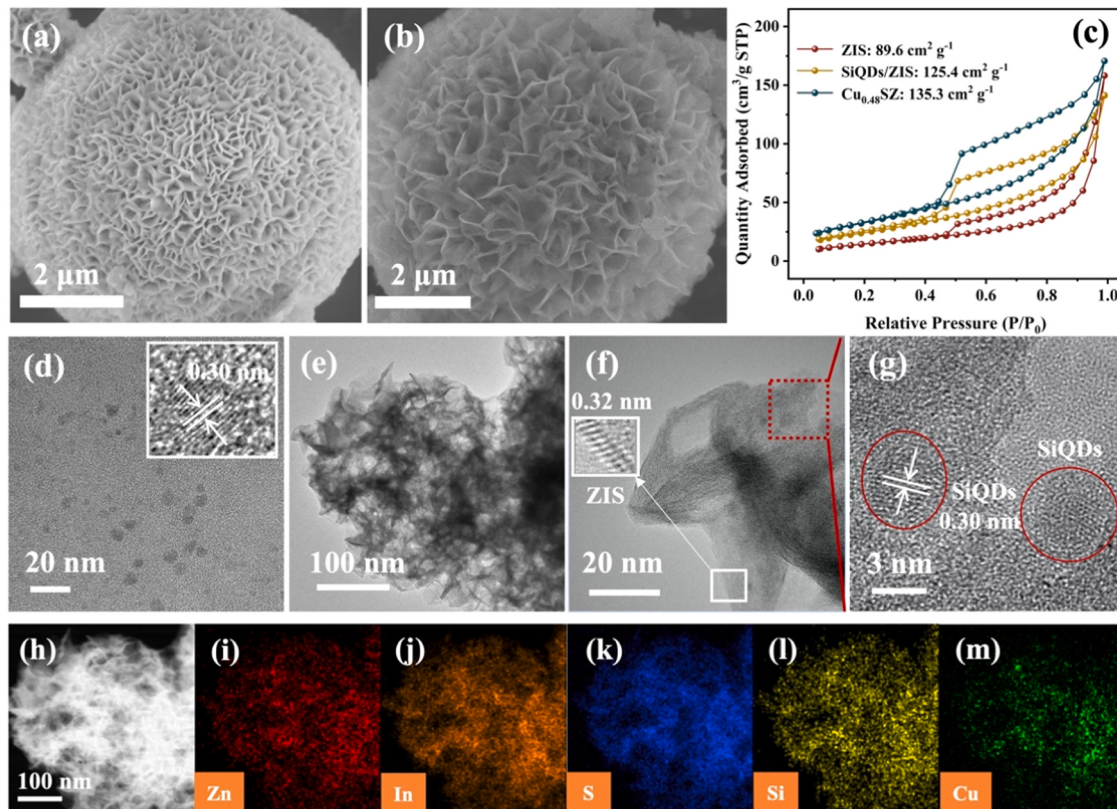


Fig. 2. Morphology characterizations. SEM images of (a) ZIS and (b) SiQDs/ZIS. (c) Nitrogen adsorption–desorption isotherms of ZIS, SiQDs/ZIS and $Cu_{0.48}SZ$. (d) TEM images of SiQDs and the corresponding HRTEM images (inset). (e) TEM and (f) HRTEM (inset: a magnified area for characteristic lattice fringes of the $ZnIn_2S_4$ outer layer) images of $Cu_{0.48}SZ$. (g) Magnified TEM image of the region of (f) boxed in red. (h-m) HAADF-STEM image of $Cu_{0.48}SZ$ and the corresponding EDX elemental mapping for Zn, In, S, Si and Cu, respectively.

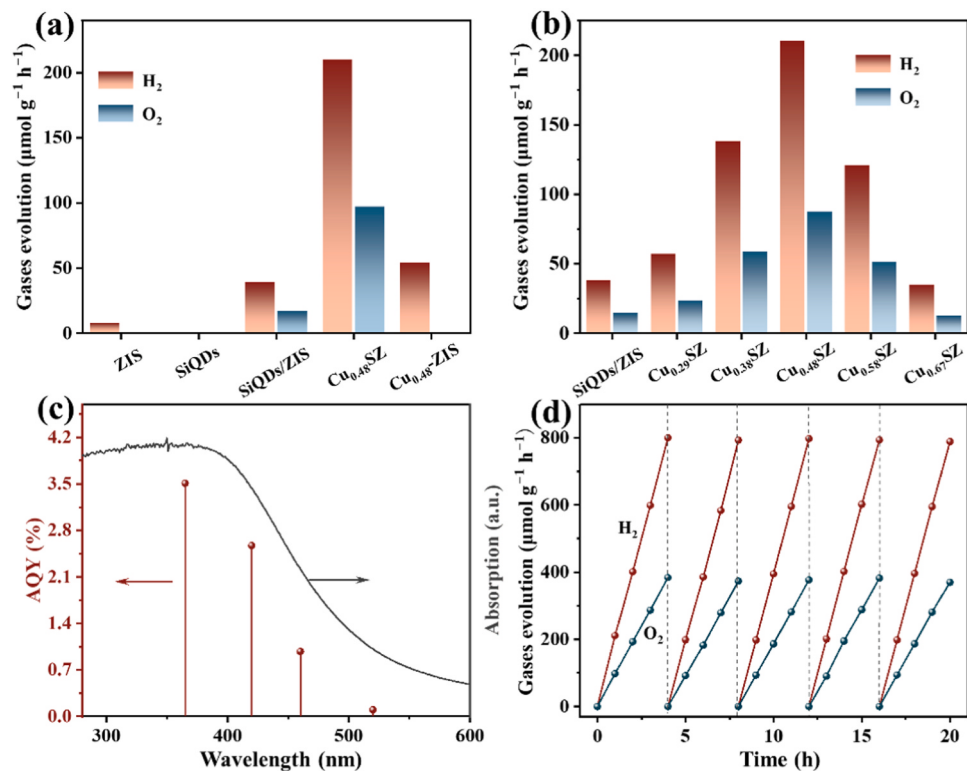


Fig. 3. Photocatalytic performance under visible-light illumination. (a) Comparison of the H_2 - and O_2 -evolution activities of ZIS, SiQDs, SiQDs/ZIS, $\text{Cu}_{0.48}\text{SZ}$ and $\text{Cu}_{0.48}\text{-ZIS}$ (without SiQDs) in photocatalytic water-splitting reaction. (b) Photocatalytic activity of Cu_xSZ ($X = 0.29, 0.38, 0.48, 0.58$, and 0.67). (c) UV-visible absorption and wavelength-dependent AQYs of $\text{Cu}_{0.48}\text{SZ}$ and (d) cycling stability test.

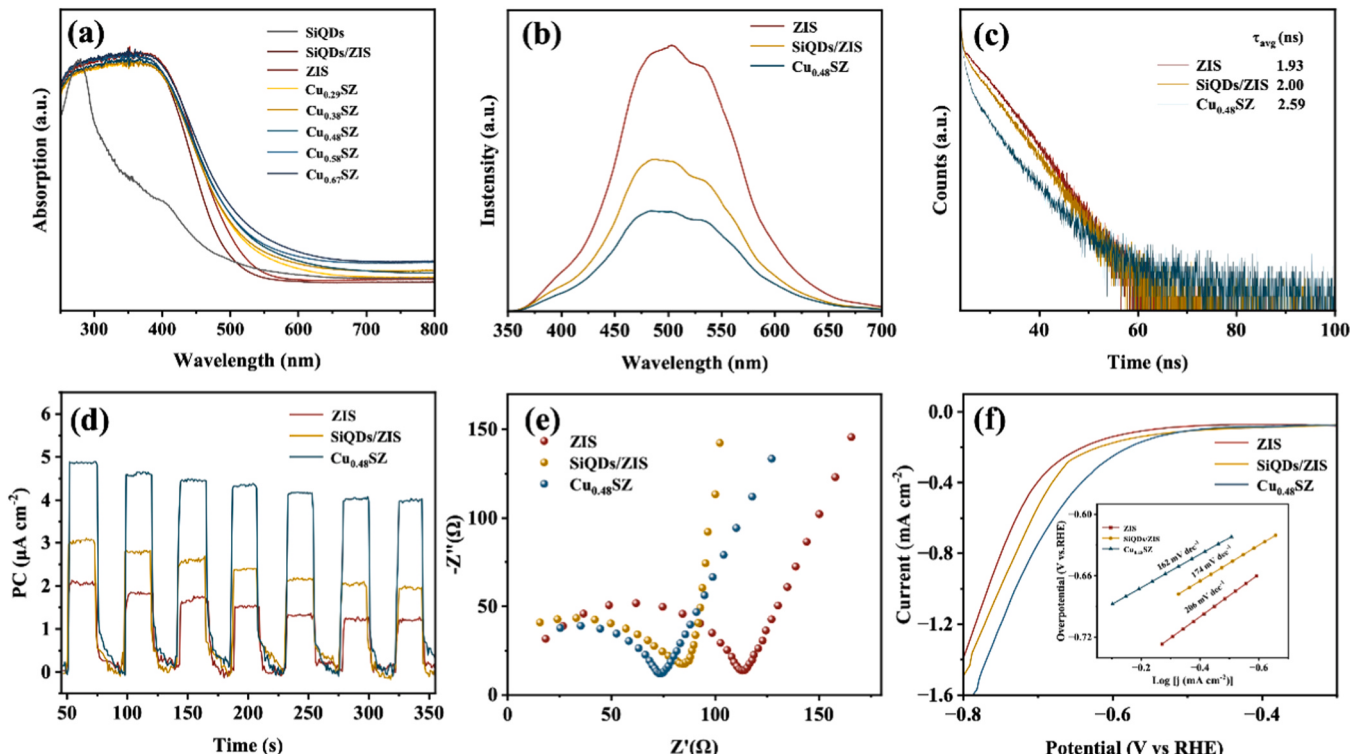


Fig. 4. Photophysical and electrochemical measurements. (a) UV-visible DRS of SiQDs, ZIS and Cu_xSZ ($X = 0.29, 0.38, 0.48, 0.58$, and 0.67). (b) Steady-state PL spectra, (c) time-resolved PL decay, (d) periodic (on/off) photocurrent responses, (e) EIS plots, and (f) LSV curves for HER (inset: Tafel plots) of ZIS, SiQDs/ZIS and $\text{Cu}_{0.48}\text{SZ}$ samples.

indicate that SiQDs can effectively prevent self-oxidation of ZIS and act as efficient hole transporter to boost redox process. Moreover, by optimizing the loading amounts of SiQDs (Fig. S11) and Cu doping (Fig. 4b), the Cu_{0.48}SZ sample achieves the highest overall water-splitting activity with the H₂- and O₂-evolution rates of 210 and 97 $\mu\text{mol g}^{-1} \text{h}^{-1}$, respectively, superior to most reported ZIS-based photocatalysts (Table S4). We also measured the apparent quantum yield (AQY) of Cu_{0.48}SZ at different wavelengths ($\lambda=365$ nm, 420 nm, 480 nm and 520 nm) (Fig. 4c). The AQY at 420 nm was determined to be 2.57 %, which is better than those reported in most literature (Table S4). In addition, the trend of AQY values matches well with the optical absorption curve, suggesting that the water-splitting reaction over Cu_{0.48}SZ is driven by the absorbed photons, which can be confirmed by the control experiments (Fig. S15). Furthermore, Fig. S16 illustrates that the usage of catalyst (10 mg) in the photocatalytic reaction is appropriate.

The cycling experiments (Fig. 4d) display excellent photocatalytic stability and durability of Cu_{0.48}SZ. Besides, the crystal structure and morphology of Cu_{0.48}SZ kept stable after photocatalytic reaction (Fig. S15). No obvious peak shift was observed for the regional XPS spectra of Zn, In, S, Si, and Cu after photocatalytic reaction (Fig. S16), indicating the stable chemical compositions and valence states during photocatalysis.

3.3. Photoelectrochemical and surface properties analysis

The separation and migration process of photoexcited charges was investigated by photoelectrochemical characterization. Fig. 4a depicts the UV-vis absorption spectra of the samples. With the increasing Cu content, the light-harvesting capability of Cu_xSZ gradually increases, along with a change in sample color from yellow to yellowish-brown [33]. From Tauc plots, the band positions of ZIS, SiQDs/ZIS and Cu_{0.48}SZ can reach 2.82, 2.83 and 2.86 eV, respectively (Fig. S17). The positions of conduction band (E_{CB}) and valence band (E_{VB}) across the redox potentials of H₂O fulfill the requirements for photocatalytic overall water splitting. The loading of SiQDs greatly reduces the PL intensity, especially for Cu_{0.48}SZ (Fig. 4b), suggesting that the recombination of photoinduced electron–hole pairs is substantially inhibited. The lifetime of photogenerated carriers was investigated by time-resolved transient fluorescence spectroscopy (Fig. 4c). Cu_{0.48}SZ has a longer average lifetime (τ_{avg}) (2.59 ns) than SiQDs/ZIS (2.00 ns) and ZIS (1.93 ns), meaning that ZIS modified by both SiQDs and Cu²⁺ possesses a longer lifetime of photogenerated carriers than pure ZIS. In response to this, Cu_{0.48}SZ presents the strongest photocurrent signals (Fig. 4d), reflecting a better photocarrier separation/migration efficiency. In addition, the Cu_{0.48}SZ sample manifests a lower electrical resistance than SiQDs/ZIS and ZIS according to Nyquist plots through the electrochemical impedance (EIS) test (Fig. 4e). Similarly, the curves of the linear sweep voltammetry (LSV) of Cu_{0.48}SZ and SiQDs/ZIS have higher cathode current density and lower overpotential than ZIS (Fig. 4f). This result further proves that the introduction of SiQDs and Cu²⁺ can prompt the separation of photogenerated electron–hole pairs. Moreover, by transforming LSV curves into the corresponding Tafel slopes in the low current density region, a smaller Tafel slope for Cu_{0.48}SZ indicates a faster kinetic process, meaning that the catalyst can reach the required current at a lower overpotential [49]. The photoelectrochemical results demonstrate that the synergy of SiQDs and Cu²⁺ plays a crucial role in charge transfer and separation, allowing more photoexcited charge carriers to actively participate in redox reactions.

Based on the cyclic voltammetry (CV) curves (Fig. S18d), the calculated double-layer capacitances (C_{dl}) of Cu_{0.48}SZ (0.069 mF cm⁻²) and SiQDs/ZIS (0.060 mF cm⁻²) are higher than that of ZIS (0.031 mF cm⁻²), confirming that Cu_{0.48}SZ and SiQDs/ZIS have larger electrochemical surface area than ZIS. The larger electrochemical and BET surface area of Cu_{0.48}SZ provides more active sites for catalytic reactions. Moreover, water contact angle tests were used to investigate the

hydrophilicity of the photocatalyst surface. In Fig. S19, the smallest water contact angle indicates that Cu_{0.48}SZ possesses higher hydrophilicity than SiQDs and ZIS, which is helpful for the adsorption and activation of H₂O molecules [50].

3.4. Mechanism analysis

Electron paramagnetic resonance (EPR) spin-trapping technique is often used to record the major radicals of the photocatalytic reduction reaction. Fig. 5a proves that Cu_{0.48}ZIS and Cu_{0.48}SZ produce more superoxide radical ($\bullet\text{O}_2^-$) than pristine ZIS and SiQDs/ZIS under lighting condition, which suggests that the Cu doping effectively accelerates the water-reduction reaction [47]. Improved charge-transfer ability can also be evidenced by surface photovoltage (SPV) spectra (Fig. 5b). The positive SPV responses reveal that photoinduced holes migrate to the semiconductor surface under illumination, rendering a characteristic of n-type semiconductors [51]. The more positive the SPV signal, the charge separation is more efficient for n-type semiconductors. Besides, the SPV response of SiQDs/ZIS is obviously higher than that of ZIS, meaning that SiQDs mediate the transport of holes to the surface. Therefore, the presence of SiQDs boosts the hole transfer from ZIS for water-oxidation reactions and effectively avoids self-oxidation of ZIS.

Fig. 5c exhibits the optimal structure of Cu_{0.48}SZ after Zn atoms replace Cu atoms on the surface of ZIS. The optimized structures of ZIS and SiQDs/ZIS are also given in Fig. S20. Charge density difference analysis was carried out to study the electron distribution. Fig. 5d, e shows the charge density difference of Cu_{0.48}SZ, where the yellow and green contours denote the accumulation and depletion of electron density, respectively. The location of SiQDs displays electron deficiency because of the hole transfer from ZIS to SiQDs (Fig. 5b), which further demonstrates that photoexcited holes are transferred onto the surface of SiQDs for water oxidation. Moreover, the prominent electron transfer occurs from SiQDs to the S atoms of ZIS, causing electron accumulation at the S sites. According to Bader charge calculations, the amount of charge transfer was quantified. The average charge in Cu_{0.48}SZ (-0.62 e) is more negative than that of SiQDs/ZIS (-0.58 e) (Fig. 5d and Fig. S21), confirming that the Cu doping is beneficial to the accumulation of electrons at the S sites. This result is consistent with the XPS analysis. The increase of electron cloud density in the neighboring S atoms is due to the charge redistribution caused by the partial substitution of Zn atoms by Cu atoms. Furthermore, to deeply explore the mechanism on the enhanced photocatalytic activity of Cu_{0.48}SZ, water reduction/oxidation reaction paths were theoretically calculated for ZIS, SiQDs/ZIS and Cu_{0.48}SZ samples with free energy diagrams (Fig. 5f, g). In general, the free energy of hydrogen adsorption ($|\Delta G^*_{\text{H}}|$) should be close to zero, favoring the H⁺ adsorption on the surface and the H/H₂ desorption from the surface [52]. For pure ZIS, a ΔG^*_{H} value of 0.40 eV is required for the formation of *H to H₂. After the introduction of SiQDs onto ZIS, the $|\Delta G^*_{\text{H}}|$ decreased to 0.30 eV due to the improved separation and migration of carriers on the surface. By comparison, the Cu_{0.48}SZ sample holds the smallest $|\Delta G^*_{\text{H}}|$ value of 0.15 eV. This is because the electron accumulates on the S atoms by Cu doping and the resulting activation of S atoms is more favorable for *H adsorption with a lower HER barrier. In addition, the evolution of three intermediates (*O, *OH and *OOH) formed during OER was further calculated using Gibbs free energy (Fig. 5g). The largest Gibbs free energy difference ($\Delta G = 2.11$ eV, corresponding to $\eta_{\text{OER}} = 0.88$ V) of the basal (110) plane of pristine ZIS occurs in the process of *O to *OOH, meaning that the strong adsorption of *OOH on ZIS is the potential-determining step (PDS) in the OER process. SiQDs/ZIS has a lower η_{OER} (0.61 V) for the PDS (the formation process from *OH to *O) than that of ZIS, illustrating that SiQDs lower the energy required for the OER process. Besides, the PDS is also the formation process from *OH to *O for Cu_{0.48}SZ while the η_{OER} decreases to 0.42 V, suggesting that SiQDs and Cu doping can lower the OER energy barrier for H₂O oxidation synergistically [53].

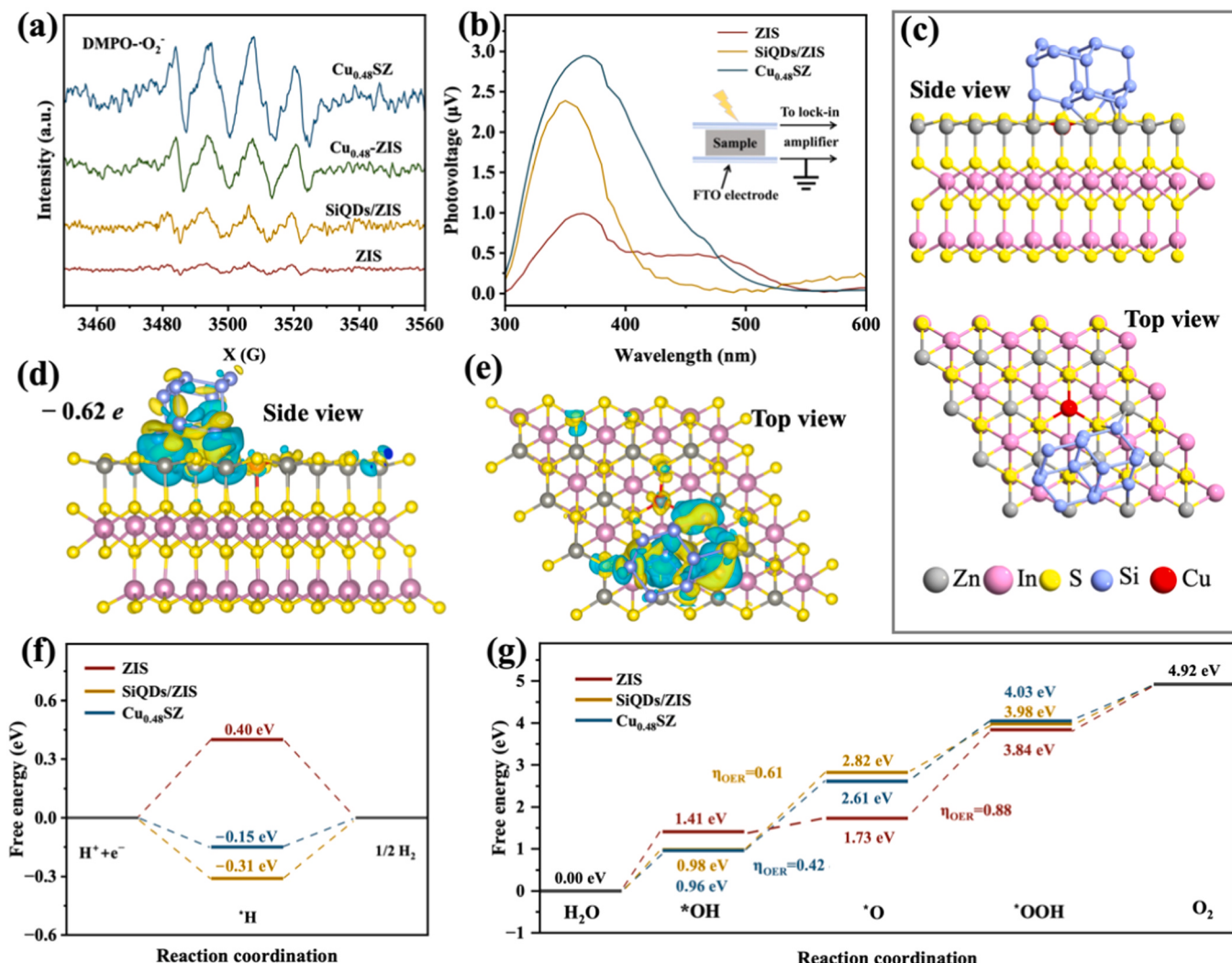


Fig. 5. Water-splitting mechanism. (a) DMPO spin-trapping EPR spectra of DMPO-•O₂⁻ for ZIS, SiQDs/ZIS, Cu_{0.48}ZIS and Cu_{0.48}SZ in methanol solution. (b) SPV of ZIS, SiQDs/ZIS and Cu_{0.48}SZ. The inset describes the schematic setup for measurements. (c) Optimized structure, (d) side view and (e) top view of charge density difference of Cu_{0.48}SZ. Calculated free energy diagrams of (f) HER and (g) OER for ZIS, SiQDs/ZIS and Cu_{0.48}SZ.

4. Conclusions

In summary, we present SiQDs for the first time for use as efficient photoexcited hole transporter and have successfully constructed SiQDs/Cu-doped ZnIn₂S₄ heterojunction for photocatalytic overall water splitting. The well-established Cu_{0.48}SZ sample exhibits remarkable performance in overall photocatalytic water splitting with 210 $\mu\text{mol g}^{-1} \text{h}^{-1}$ H₂-production rate and 97 $\mu\text{mol g}^{-1} \text{h}^{-1}$ O₂-production rate, and an AQY of 2.57 % at 420 nm. These values are quite competitive with the most of previous ZIS-based photocatalysts. Experimental and theoretical investigations corroborated that the introduction of SiQDs can accelerate hole transfer to adsorbed H₂O molecules during the OER process and effectively avoid the instability of metal sulfide photocatalysts, while the Cu doping contributes to accumulating electron density on the neighboring S atoms with more active H⁺ adsorption for the HER process. Besides, better hydrophilicity of Cu_{0.48}SZ promotes the adsorption and migration of H₂O molecules and its intermediates on the surface. This work provides new insights for the applications of SiQDs in photocatalysis and designing highly stable and efficient metal sulfide photocatalysts for overall water splitting.

CRediT authorship contribution statement

Wenwen Shi: Writing – original draft, Visualization, Investigation, Formal analysis, Data curation. **Baoxin Ge:** Writing – review & editing, Software. **Pengyang Jiang:** Writing – review & editing. **Caijin Huang:** Writing – review & editing, Supervision, Resources, Funding acquisition, Conceptualization. **Qiaoyun Wang:** Writing – review & editing. **Lifeng He:** Writing – review & editing.

Author contributions

C.J.H. and S.W.W designed the whole experiment and co-wrote the manuscript. **S.W.W.** performed the experimental measurements and experimental data analysis. **G.B.X** contributed to the DFT calculation. All authors commented and approved the paper.

Declaration of Competing Interest

The authors declare that they have no known competing financial interests or personal relationships that could have appeared to influence the work reported in this paper.

Data availability

The authors do not have permission to share data.

Acknowledgements

This work was supported by the National Natural Science Foundation of China (grant no. 22072024).

Appendix A. Supporting information

Supplementary data associated with this article can be found in the online version at [doi:10.1016/j.apcatb.2024.124121](https://doi.org/10.1016/j.apcatb.2024.124121).

References

- [1] B. Dai, J. Fang, Y. Yu, M. Sun, H. Huang, C. Lu, J. Kou, Y. Zhao, Z. Xu, Construction of infrared-light-responsive photoinduced carriers driver for enhanced photocatalytic hydrogen evolution, *Adv. Mater.* 32 (2020) 1906361.
- [2] T. Hisatomi, K. Domen, Reaction systems for solar hydrogen production via water splitting with particulate semiconductor photocatalysts, *Nat. Catal.* 2 (2019) 387–399.
- [3] Y.P. Zhu, J. Yin, E. Abou-Hamad, X. Liu, W. Chen, T. Yao, O.F. Mohammed, H. N. Alshareef, Highly stable phosphonate-based MOFs with engineered bandgaps for efficient photocatalytic hydrogen production, *Adv. Mater.* 32 (2020) 1906368.
- [4] S. Zhang, X. Liu, C. Liu, S. Luo, L. Wang, T. Cai, Y. Zeng, J. Yuan, W. Dong, Y. Pei, Y. Liu, MoS_2 quantum dot growth induced by S vacancies in a ZnIn_2S_4 monolayer: atomic-level heterostructure for photocatalytic hydrogen production, *ACS Nano* 12 (2018) 751–758.
- [5] Q. Zhu, Z. Xu, B. Qiu, M. Xing, J. Zhang, Emerging cocatalysts on $\text{g-C}_3\text{N}_4$ for photocatalytic hydrogen evolution, *Small* 17 (2021) 2101070.
- [6] J. Xu, X. Li, Z. Ju, Y. Sun, X. Jiao, J. Wu, C. Wang, W. Yan, H. Ju, J. Zhu, Y. Xie, Visible-light-driven overall water splitting boosted by tetrahedrally coordinated blende cobalt(II) oxide atomic layers, *Angew. Chem. Int. Ed.* 58 (2019) 3032–3036.
- [7] Y. Zhao, R. Nakamura, K. Kamiya, S. Nakanishi, K. Hashimoto, Nitrogen-doped carbon nanomaterials as non-metal electrocatalysts for water oxidation, *Nat. Commun.* 4 (2013) 2390.
- [8] X. Yan, M. Xia, H. Liu, B. Zhang, C. Chang, L. Wang, G. Yang, An electron-hole rich dual-site nickel catalyst for efficient photocatalytic overall water splitting, *Nat. Commun.* 14 (2023) 1741.
- [9] N. Srinivasan, E. Sakai, M. Miyachi, Balanced excitation between two semiconductors in bulk heterojunction Z-scheme system for overall water splitting, *ACS Catal.* 6 (2016) 2197–2200.
- [10] K. Takanabe, Photocatalytic water splitting: quantitative approaches toward photocatalyst by design, *ACS Catal.* 7 (2017) 8006–8022.
- [11] F. Wang, A. Dong, W.E. Buhro, Solution-liquid-solid synthesis, properties, and applications of one-dimensional colloidal semiconductor nanorods and nanowires, *Chem. Rev.* 116 (2016) 10888–10933.
- [12] C. Zhang, Z.C. Shao, X.L. Zhang, G.Q. Liu, Y.Z. Zhang, L. Wu, C.Y. Liu, Y. Pan, F. H. Su, M.R. Gao, Y. Li, S.H. Yu, Design principles for maximizing hole utilization of semiconductor quantum wires toward efficient photocatalysis, *Angew. Chem. Int. Ed.* 62 (2023) 202305571.
- [13] W. Bi, X. Li, L. Zhang, T. Jin, L. Zhang, Q. Zhang, Y. Luo, C. Wu, Y. Xie, Molecular co-catalyst accelerating hole transfer for enhanced photocatalytic H_2 evolution, *Nat. Commun.* 6 (2015) 8647.
- [14] J. Liu, J. Ke, Y. Li, B. Liu, L. Wang, H. Xiao, S. Wang, Co_3O_4 quantum dots/ TiO_2 nanobelt hybrids for highly efficient photocatalytic overall water splitting, *Appl. Catal. B Environ.* 236 (2018) 396–403.
- [15] J. Wu, Z. Liu, X. Lin, E. Jiang, S. Zhang, P. Huo, Y. Yan, P. Zhou, Y. Yan, Breaking through water-splitting bottlenecks over carbon nitride with fluorination, *Nat. Commun.* 13 (2022) 6999.
- [16] X. Xin, Y. Li, Y. Zhang, Y. Wang, X. Chi, Y. Wei, C. Diao, J. Su, R. Wang, P. Guo, J. Yu, J. Zhang, A.J. Sobrido, M.M. Titirici, X. Li, Large electronegativity differences between adjacent atomic sites activate and stabilize ZnIn_2S_4 for efficient photocatalytic overall water splitting, *Nat. Commun.* 15 (2024) 337.
- [17] Y. Yan, Z. Chen, X. Cheng, W. Shi, Research progress of ZnIn_2S_4 -based catalysts for photocatalytic overall water splitting, *Catal.* 13 (2023) 967–993.
- [18] H. Jing, J. Ren, J. Yue, S. Liu, Q. Liang, R. Wu, Y. Wang, Z. Fang, H. Li, S. Wei, ZnIn_2S_4 with oxygen atom doping and surface sulfur vacancies for overall water splitting under visible light irradiation, *Catal. Sci. Technol.* 13 (2023) 226–232.
- [19] W.K. Chong, B.J. Ng, Y.J. Lee, L.L. Tan, L.K. Putri, J. Low, A.R. Mohamed, S. P. Chai, Self-activated superhydrophilic green ZnIn_2S_4 realizing solar-driven overall water splitting: close-to-unity stability for a full daytime, *Nat. Commun.* 14 (2023) 7676.
- [20] R. Pan, M. Hu, J. Liu, D. Li, X. Wan, H. Wang, Y. Li, X. Zhang, X. Wang, J. Jiang, J. Zhang, Two-dimensional all-in-one sulfide monolayers driving photocatalytic overall water splitting, *Nano. Lett.* 21 (2021) 6228–6236.
- [21] Y. Xu, Z. Zhou, P. Yu, Y. Wang, Al-doped $\text{CuS}/\text{ZnIn}_2\text{S}_4$ forming Schottky junction induced electron trap centers for photocatalytic overall water splitting, *Chem. Eng. J.* 470 (2023) 144275–144283.
- [22] G. Zuo, W. Chen, Z. Yin, S. Ma, Y. Wang, Q. Ji, Q. Xian, S. Yang, H. He, Covalency dominating Z-scheme perylene-dicarboximide@ ZnIn_2S_4 organic-inorganic hybrids for overall water splitting, *Chem. Eng. J.* 456 (2023) 141096.
- [23] B. Sun, J. Bu, X. Chen, D. Fan, S. Li, Z. Li, W. Zhou, Y. Du, In-situ interstitial zinc doping-mediated efficient charge separation for ZnIn_2S_4 nanosheets visible-light photocatalysts towards optimized overall water splitting, *Chem. Eng. J.* 435 (2022) 135074–135174.
- [24] B. Sun, D. Fan, X. Chen, Z. Li, W. Zhou, Y. Du, Heteroatom-induced domain electrostatic potential difference in ZnIn_2S_4 nanosheets for efficient charge separation and boosted photocatalytic overall water splitting, *Mater. Chem. Front.* 6 (2022) 1795–1802.
- [25] F. Li, Y. Liu, B. Mao, L. Li, H. Huang, D. Zhang, W. Dong, Z. Kang, W. Shi, Carbon-dots-mediated highly efficient hole transfer in I-III-VI quantum dots for photocatalytic hydrogen production, *Appl. Catal. B Environ.* 292 (2021) 120154.
- [26] Q. Chen, Y. Liu, B. Mao, Z. Wu, W. Yan, D. Zhang, Q. Li, H. Huang, Z. Kang, W. Shi, Carbon-dot-mediated highly efficient visible-driven photocatalytic hydrogen evolution coupled with organic oxidation, *Adv. Funct. Mater.* 33 (2023) 2305318.
- [27] X. Cheng, E. Hinde, D.M. Owen, S.B. Lowe, P.J. Reece, K. Gaus, J.J. Gooding, Enhancing quantum dots for bioimaging using advanced surface chemistry and advanced optical microscopy: application to silicon quantum dots (SiQDs), *Adv. Mater.* 27 (2015) 6144–6150.
- [28] M.J. Kloberg, H. Yu, E. Gross, F. Eckmann, T.M.F. Restle, T.F. Fassler, J.G. C. Veinot, B. Rieger, Surface-anisotropic janus silicon quantum dots via masking on 2D silicon nanosheets, *Adv. Mater.* 33 (2021) 2100288.
- [29] J. Wu, J. Dai, Y. Shao, Y. Sun, One-step synthesis of fluorescent silicon quantum dots (Si-QDs) and their application for cell imaging, *Rsc. Adv.* 5 (2015) 83581–83587.
- [30] L. Lu, R. Zeng, Q. Lin, X. Huang, D. Tang, Cation exchange reaction-mediated photothermal and polarity-switchable photoelectrochemical dual-readout biosensor, *Anal. Chem.* 95 (2023) 16335–16342.
- [31] L. De Trizio, L. Manna, Forging colloidal nanostructures via cation exchange reactions, *Chem. Rev.* 116 (2016) 10852–10887.
- [32] X. Shi, L. Mao, C. Dai, P. Yang, J. Zhang, F. Dong, L. Zheng, M. Fujitsuka, H. Zheng, Inert basal plane activation of two-dimensional ZnIn_2S_4 via Ni atom doping for enhanced co-catalyst free photocatalytic hydrogen evolution, *J. Mater. Chem. A* 8 (2020) 13376–13384.
- [33] P. Wang, Z. Shen, Y. Xia, H. Wang, L. Zheng, W. Xi, S. Zhan, Atomic insights for optimum and excess doping in photocatalysis: a case study of few-layer $\text{Cu-ZnIn}_2\text{S}_4$, *Adv. Funct. Mater.* 29 (2018) 1807013.
- [34] R. Rameshababu, P. Ravi, M. Sathish, Cauliflower-like CuS/ZnS nanocomposites decorated $\text{g-C}_3\text{N}_4$ nanosheets as noble metal-free photocatalyst for superior photocatalytic water splitting, *Chem. Eng. J.* 360 (2019) 1277–1286.
- [35] Y. Li, S. Li, L. Meng, S. Peng, Synthesis of oriented J type $\text{ZnIn}_2\text{S}_4/\text{CdIn}_2\text{S}_4$ heterojunction by controllable cation exchange for enhancing photocatalytic hydrogen evolution, *J. Colloid Inter. Sci.* 650 (2023) 266–274.
- [36] Y. Zhong, F. Peng, F. Bao, S. Wang, X. Ji, L. Yang, Y. Su, S.T. Lee, Y. He, Large-scale aqueous synthesis of fluorescent and biocompatible silicon nanoparticles and their use as highly photostable biological probes, *J. Am. Chem. Soc.* 135 (2013) 8350–8356.
- [37] K. Dohnalová, A.N. Poddubny, A.A. Prokofiev, W.D.A.M. de Boer, C.P. Umesh, J.M. J. Paulusse, H. Zuilhof, T. Gregorkiewicz, Surface brightens up Si quantum dots: direct bandgap-like size-tunable emission, *Light Sci. Appl.* 2 (2013) 47.
- [38] J. Neugebauer, M. Scheffler, Adsorbate-substrate and adsorbate-adsorbate interactions of Na and K adlayers on Al(111), *Phys. Rev. B Condens. Matter* 46 (1992) 16067–16080.
- [39] P.E. Blochl, Projector augmented-wave method, *Phys. Rev. B Condens. Matter* 50 (1994) 17953–17979.
- [40] G. Henkelman, A. Arnaldsson, H. Jónsson, A fast and robust algorithm for Bader decomposition of charge density, *Comp. Mater. Sci.* 36 (2006) 354–360.
- [41] Q. Liu, M. Wang, Y. He, X. Wang, W. Su, Photochemical route for synthesizing Co-P alloy decorated ZnIn_2S_4 with enhanced photocatalytic H_2 production activity under visible light irradiation, *Nanoscale* 10 (2018) 19100–19106.
- [42] B. Jana, Y. Reva, T. Scharl, V. Strauss, A. Cadrelan, D.M. Guldi, Carbon nanodots for all-in-one photocatalytic hydrogen generation, *J. Am. Chem. Soc.* 143 (2021) 20122–20132.
- [43] F. Xing, R. Zeng, C. Cheng, Q. Liu, C. Huang, POM-incorporated ZnIn_2S_4 Z-scheme dual-functional photocatalysts for cooperative benzyl alcohol oxidation and H_2 evolution in aqueous solution, *Appl. Catal. B Environ.* 306 (2022) 121087.
- [44] J. Xie, Z. Li, X. Zheng, F. Tian, D. Lei, C. Wang, Built-In electric field of in situ formed artificial interface layer induces fast and uniform sodium-ions transmission to achieve a long-term stable sodium metal battery under harsh conditions, *Adv. Funct. Mater.* (2024) 2315309.
- [45] W. Jin, Z. Chen, Y. Wang, J. Li, J. Li, Y. Pei, Z. Pei, Nano metal-photosensitizer based on Aza-BODIPY-Cu complex for CDT-enhanced dual phototherapy, *Chin. Chem. Lett.* (2023) 109328.
- [46] J. Wu, Y. Feng, Y. Shao, J. Zhou, X. Wu, Novel SiQDs– MoS_2 heterostructures with increasing solar absorption for the photocatalytic degradation of malachite green, *J. Mater. Sci.* 53 (2018) 8120–8131.
- [47] X. Wang, Y. Wang, J. Huang, S. Li, A. Meng, Z. Li, Interfacial chemical bond and internal electric field modulated Z-scheme $\text{Sv-ZnIn}_2\text{S}_4/\text{MoSe}_2$ photocatalyst for efficient hydrogen evolution, *Nat. Commun.* 12 (2021) 4112–4123.
- [48] G. Zuo, Y. Wang, W.L. Teo, Q. Xian, Y. Zhao, Direct Z-scheme TiO_2 – ZnIn_2S_4 nanoflowers for cocatalyst-free photocatalytic water splitting, *Appl. Catal. B Environ.* 291 (2021) 120126.

[49] F.-T. Tsai, Y.-T. Deng, C.-W. Pao, J.-L. Chen, J.-F. Lee, K.-T. Lai, W.-F. Liaw, The HER/OER mechanistic study of an FeCoNi-based electrocatalyst for alkaline water splitting, *J. Mater. Chem. A* 8 (2020) 9939–9950.

[50] B. Lin, G. Yang, L. Wang, Stacking-layer-number dependence of water adsorption in 3D ordered close-packed g-C₃N₄ nanosphere arrays for photocatalytic hydrogen evolution, *Angew. Chem. Int. Ed.* 58 (2019) 4587–4591.

[51] D. Zhao, Y. Wang, C.-L. Dong, Y.-C. Huang, J. Chen, F. Xue, S. Shen, L. Guo, Boron-doped nitrogen-deficient carbon nitride-based Z-scheme heterostructures for photocatalytic overall water splitting, *Nat. Energy* 6 (2021) 388–397.

[52] H. Wang, Y. Xia, H. Li, X. Wang, Y. Yu, X. Jiao, D. Chen, Highly active deficient ternary sulfide photoanode for photoelectrochemical water splitting, *Nat. Commun.* 11 (2020) 3078.

[53] D. Zhao, Y. Wang, C.L. Dong, F. Meng, Y.C. Huang, Q. Zhang, L. Gu, L. Liu, S. Shen, Electron-deficient Zn-N₆ configuration enabling polymeric carbon nitride for visible-light photocatalytic overall water splitting, *Nano Micro Lett.* 14 (2022) 223.